

See discussions, stats, and author profiles for this publication at: <https://www.researchgate.net/publication/231647427>

Glucose-Assisted One-Pot Synthesis of FeOOH Nanorods and Their Transformation to Fe₃O₄@Carbon Nanorods for Application in Lithium Ion Batteries

ARTICLE in THE JOURNAL OF PHYSICAL CHEMISTRY C · APRIL 2011

Impact Factor: 4.77 · DOI: 10.1021/jp2013754

CITATIONS

126

READS

35

3 AUTHORS, INCLUDING:



Ting Zhu

National University of Singapore

24 PUBLICATIONS 1,575 CITATIONS

SEE PROFILE



Jun Song Chen

Nanyang Technological University

56 PUBLICATIONS 6,489 CITATIONS

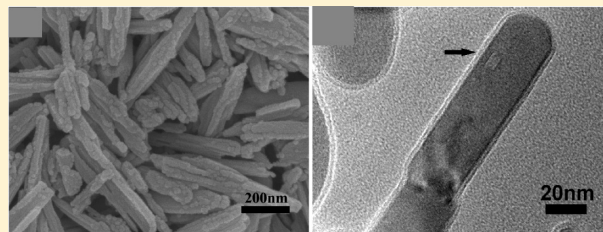
SEE PROFILE

Glucose-Assisted One-Pot Synthesis of FeOOH Nanorods and Their Transformation to Fe₃O₄@Carbon Nanorods for Application in Lithium Ion Batteries

Ting Zhu, Jun Song Chen, and Xiong Wen (David) Lou*

School of Chemical and Biomedical Engineering, Nanyang Technological University, 70 Nanyang Drive, Singapore 637457, Singapore

ABSTRACT: In this work, we demonstrate a facile one-pot glucose-mediated hydrothermal method for the synthesis of ferric oxyhydroxide (FeOOH) rodlike nanoparticles. It is found that the presence of glucose not only facilitates the formation of FeOOH nanorods but also gives rise to a uniform, glucose-derived, carbon-rich polysaccharide (GCP) overlayer on the FeOOH nanorods. By varying the concentrations of ferric ion, the aspect ratios of these FeOOH nanorods can be readily tuned. The corresponding carbon-coated magnetite (Fe₃O₄@C) nanocomposites can be easily obtained by carbonizing the as-prepared GCP-coated FeOOH nanorods under inert atmosphere. These Fe₃O₄@C nanorods exhibit good cycling performance for lithium storage. Specifically, reversible capacities of as high as 808 mA h g⁻¹ can be retained after 100 charge–discharge cycles, making them promising anode materials for lithium ion batteries.



INTRODUCTION

In the past decades, rechargeable lithium ion batteries (LIBs) have been widely employed as the power source for various portable electronic devices.^{1–5} More recently, they are receiving increasing attention because of the rapid development of electric vehicles that can help to alleviate environment problems. To meet these market demands, intensive efforts have been made by the scientific community to develop new LIBs with more attractive features, including low cost, high energy density, and good cycling performance. Recently, different types of nanostructured metal oxides have been studied as promising anodes for LIBs because of their high energy density and long cycle life.^{6–9} Among them, iron oxides (Fe₂O₃ and Fe₃O₄) nanocrystals, which are widely used in MRI contrast agents,¹⁰ gas sensor, catalysts, and pigments,^{11,12} have been extensively investigated as electrode materials for LIBs due to their abundance and environmental benignity. However, the replacement of the commercial graphite-based anode materials with these metal oxides is hindered mainly by two issues: large initial irreversible loss and poor capacity retention over extended cycling.

It is suggested that carbon coating may be a promising way to improve the cycling performance of nanostructured electrode materials,^{13–16} and there have been a few reports on the fabrication of carbon-coated iron oxides for LIBs.^{17,18} It is hypothesized that the carbon coating has played dual roles in these electrodes during the cycling process: it can increase the electronic conductivity of the material; at the same time, the carbon layer present in the composite could work as a structural buffering layer to cushion the mechanical stress caused by the large volume change during the charge–discharge process. However, most strategies for generating such nanocomposite involve time-consuming synthetic procedures, where a separate

step is usually required to deposit the carbon layer on the surface of the presynthesized metal oxide. It is thus highly desirable to develop a straightforward synthetic route to generate such functional composite materials.

We have previously demonstrated a facile one-pot method to synthesize tin oxide (SnO₂)–carbon nanocolloids using glucose and stannates as the precursors, where glucose not only serves as the carbon source but also helps the rapid precipitation of the SnO₂ nanoparticles.¹⁹ More recently, a solvothermal route has been proposed to fabricate carbon-supported ultrathin anatase TiO₂ nanosheets, where the organic compound diethylenetriamine plays important roles in both stabilizing the (001) high-energy facets of anatase TiO₂ and also serving as the carbon precursor. Through a similar approach, we herein report a simple one-step synthesis for preparing glucose-derived, carbon-rich polysaccharide (GCP)-coated ferric oxyhydroxide (FeOOH) nanorods. The synthesis uses inexpensive iron chloride hexahydrate (FeCl₃·6H₂O) and glucose as precursors. By varying the concentrations of ferric ion ([Fe³⁺] = 0.05/0.2/0.5M, products designated as samples 1–3, respectively), the aspect ratio of the FeOOH nanorods can be readily controlled. The corresponding Fe₃O₄@C (designated as samples 1*–3*) nanorods can be directly obtained with a porous structure by carbonizing the as-prepared FeOOH nanorods under inert atmosphere. It is also shown that a certain amount of GCP is coated onto the FeOOH structure during the crystallization process and then transformed into carbon after heat treatment. We subsequently evaluate the electrochemical properties of these Fe₃O₄@C nanorods as anode

Received: February 11, 2011

Revised: March 25, 2011

Published: April 22, 2011

materials for rechargeable LIBs. Compared to other reported iron oxide counterparts,^{20,21} the as-prepared samples show promising performance with good cyclic capacity retention after prolonged cycling. Considering the easy fabrication procedure, these $\text{Fe}_3\text{O}_4@\text{C}$ nanorods may be promising candidates as potential anode materials for high-performance lithium ion batteries.

EXPERIMENT SECTION

Materials Preparation. Carbon-coated FeOOH nanorods with different aspect ratios were synthesized by a simple hydrothermal method. In a typical synthesis, 6.76 g of iron chloride hexahydrate ($\text{FeCl}_3 \cdot 6\text{H}_2\text{O}$; 98%, Alfa Aesar) and 0.18 g of

glucose (anhydrous, 99%, Alfa Aesar) were dissolved in 50 mL of deionized water. After magnetic stirring for 15 min, the clear solution was transferred to a Teflon-lined stainless steel autoclave (60 mL in volume) and then kept at 160 °C for 6 h. After cooling down naturally, the precipitate was harvested by centrifugation and washed thoroughly with water and ethanol before being dried at 60 °C for 24 h. For carbonization, a certain amount of the as-prepared powder was loaded into a tube furnace and heated under high-purity N_2 at 450 °C for 4 h.

Materials Characterization. Crystallographic phases of all the products were investigated by powder X-ray diffraction (Bruker, D8-Advance XRD, $\text{Cu K}\alpha$, $\lambda = 1.5406 \text{ \AA}$). Morphologies of samples were examined by field-emission scanning electron microscopy (FESEM; JEOL, JEM-2100F) and transmission electron microscopy (TEM; JEM-2010, 200 kV). Thermal behavior of samples was characterized by thermogravimetric analysis (TGA; Shimadzu DRG-60) at a heating rate of $5 \text{ }^\circ\text{C min}^{-1}$ from room temperature to 600 °C in a dynamic atmosphere of air (200 mL min^{-1}) using α -alumina crucibles. Measurement of specific surface area and analysis of porosity for the iron oxide products was performed through measuring N_2 adsorption–desorption isotherms at 77 K with a Quantachrome NOVA-3000 system.

Electrochemical Measurement. The electrochemical measurements were conducted using two-electrode Swagelok-type cells with lithium metal working as both counter and reference electrodes under ambient condition. The working electrodes consist of 80 wt % active materials (carbon–iron oxides composites), 10 wt % of conductivity agent (carbon black, Super-P), and 10 wt % of binder (polyvinylidene, PVDF, Aldrich). Electrolyte employed in the test was 1 M LiPF_6 in a 50:50 (w/w) mixture of ethylene carbonate and diethyl carbonate. Cell assembly was carried out in

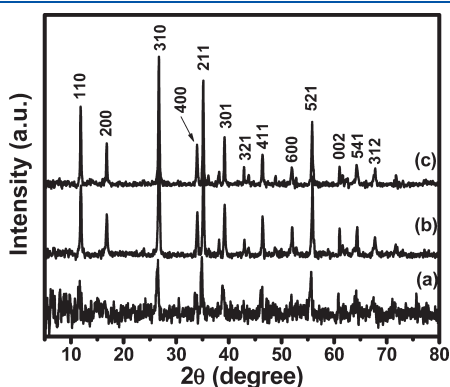


Figure 1. X-ray diffraction patterns (XRD) of the products prepared in glucose aqueous solution: (a) sample 1, (b) sample 2, and (c) sample 3.

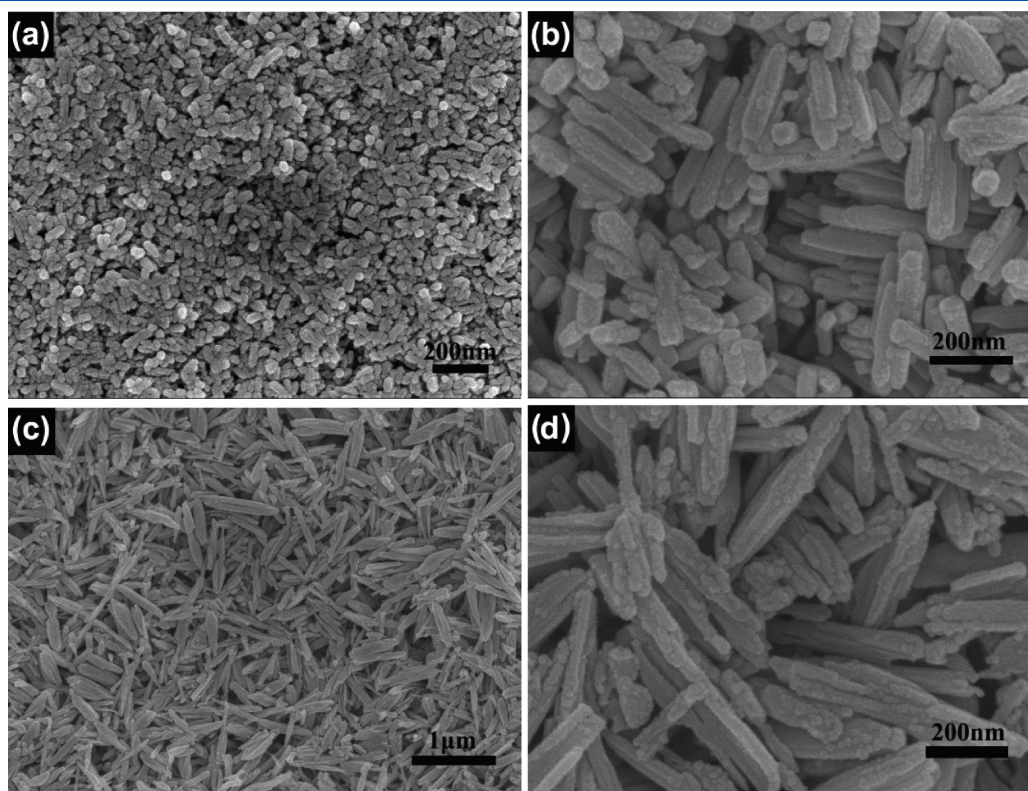


Figure 2. Field-emission scanning electron microscopy (FESEM) images of GCP-coated β - FeOOH nanorods prepared at 160 °C for 6 h with different ferric ion concentrations: (a) sample 1, $[\text{Fe}^{3+}] = 0.05 \text{ M}$; (b) sample 2, $[\text{Fe}^{3+}] = 0.2 \text{ M}$; (c, d) sample 3, $[\text{Fe}^{3+}] = 0.5 \text{ M}$.

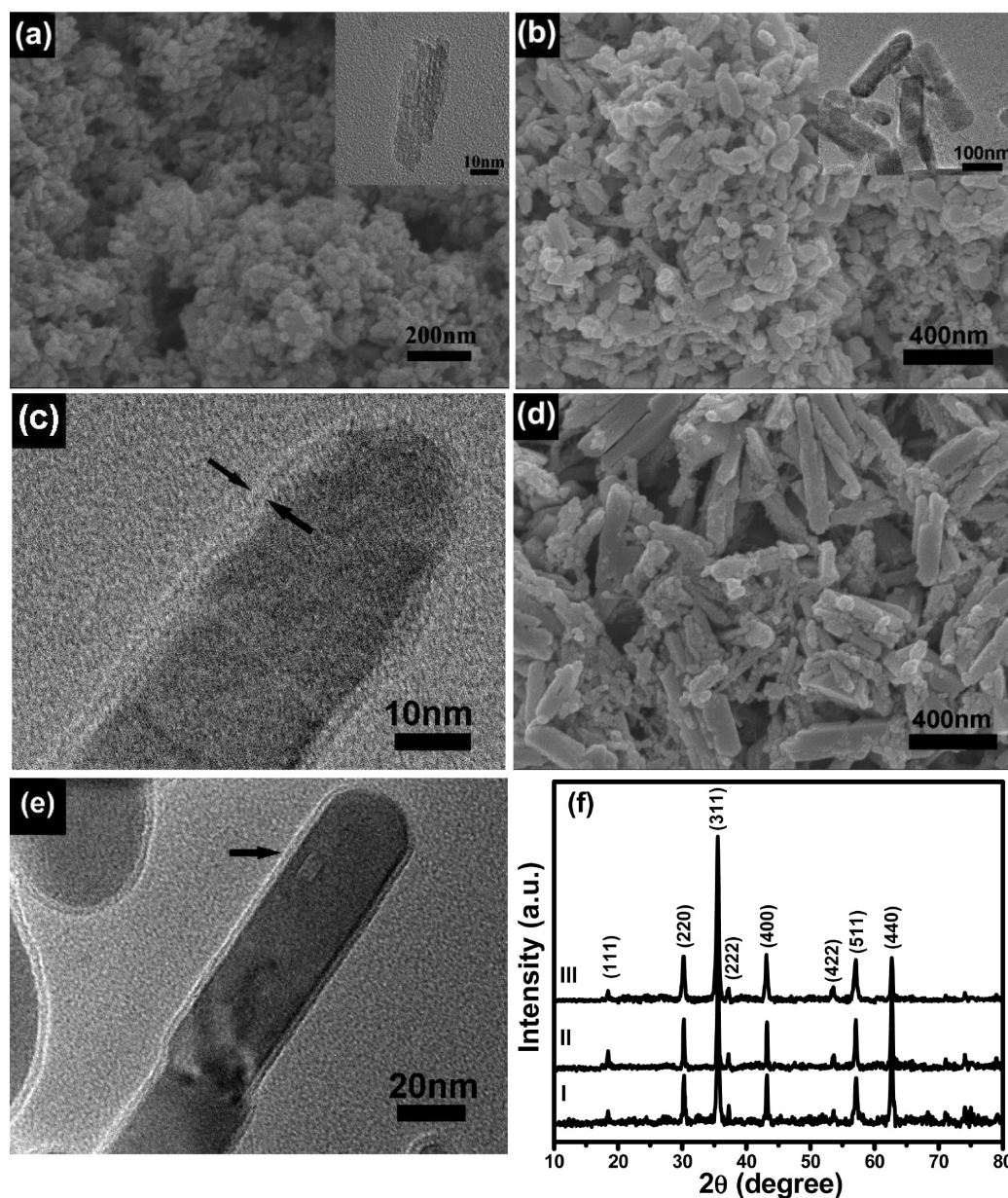


Figure 3. FESEM, transmission electron microscopy (TEM) images, and XRD patterns of iron oxides obtained by carbonizing the as-prepared β -FeOOH nanorods shown in Figure 2: (a) sample 1*, where the inset shows a TEM image of a single particle in a; (b) sample 2*, where the inset shows a TEM image of nanorods; (c) a magnified TEM image of a nanorod of sample 2*, with the carbon layer indicated by two black arrows; (d) sample 3*; (e) a magnified TEM image of a nanorod of sample 3*, with the carbon layer indicated by a black arrow; (f) I, sample 1*; II, sample 2*; III, sample 3*.

an argon-filled glovebox with both moisture and oxygen contents below 1 ppm. Cyclic voltammetry (CV, 5 mV to 3 V, 0.5 mV s^{-1}) was performed using an electrochemical workstation (CHI 660C). Galvanostatic charging/discharging was conducted on a battery test system (NEWAER).

RESULTS AND DISCUSSION

The crystal structure of as-synthesized products is determined by X-ray diffraction (XRD; Figure 1), which reveals their β -FeOOH phase (JCPDS Card No. 75-1549). It can be noted that the diffraction peaks of sample 1 are not as strong as those of samples 2 and 3, indicating its smaller crystallite size.

Figure 2 displays the β -FeOOH nanorods prepared with different concentrations of ferric ion. When the ferric ion concentration is as low as 0.05 M, small rodlike nanoparticles about 50 nm in length and 20 nm in width (Figure 2a) are produced, giving rise to an aspect ratio (defined as the length to width) of 2–3. When the $[\text{Fe}^{3+}]$ is increased to 0.2 M, most nanorods are grown with much larger dimensions. It can be seen from Figure 2b that the nanorods are grown to about 200 nm in length and about 50 nm in diameter (aspect ratio ca. 3–5). Even higher aspect ratios of ca. 5–12 of these nanorods can be achieved when the $[\text{Fe}^{3+}]$ is further increased to 0.5 M, as shown in Figure 2c,d. It can also be observed clearly from the magnified image (Figure 2d) that these long nanorods are grooved, which may be caused by the dissolution of their surface particles. It is

believed that such GCP-coated FeOOH nanorods are formed by the hydrolysis of iron chloride and the deposition of GCP simultaneously, and the glucose plays an important role on the formation of FeOOH in the reaction solution. The control experiment without glucose added shows that only hematite nanorods or quasi-nanocubes are formed (results not shown). Glucose is a hydroxyl-enriched molecule, and plenty of $-OH$ groups would be available to facilitate the FeOOH crystallization, which may be a plausible explanation for the phase transformation inhibition. Hence, it can be speculated that the presence of glucose may not only prevent the transformation of FeOOH to Fe_2O_3 , but also facilitate the rodlike structure of FeOOH.

Formation of GCP under hydrothermal conditions is a very complicated chemical process, and it is quite challenging to acquire a uniform GCP coating on preformed nanostructures

while minimizing the fraction of GCP spheres in the products.²² The present one-pot synthesis allows efficient synthesis of GCP-coated precursor nanoparticles, whose morphology largely determines the morphology of products after carbonization. Figure 3a depicts the SEM image of sample 1* (carbonized sample 1), which clearly reveals agglomeration of the rodlike nanoparticles, probably due to the fine particle size of the precursor nanoparticles. Their porous structure can be easily identified from the rough texture when viewed under TEM (Figure 3a, inset). Figure 3b shows the nanorods of sample 2* (carbonized sample 2), and the inset is a TEM image that clearly shows the rodlike structure. Figure 3c shows a single nanorod of sample 2*, where the encapsulating carbon layer can be easily observed (indicated by the two black arrows). The morphology of sample 3* (carbonized sample 3) is shown in Figure 3d. It can be observed from the image that the structure of GCP-coated FeOOH nanorods has been well-retained. The carbon overlayer on these nanorods is quite uniform, with a thickness of ~ 10 nm, as shown in Figure 3e (see black arrow). Figure 3f presents the XRD patterns of samples 1*–3*. All the identified peaks of the three samples can be attributed to magnetite iron oxide (JCPDS card No. 19-0629), indicating that the FeOOH phase in all three samples is completely converted to Fe_3O_4 at 450 °C during carbonization under N_2 . No diffraction peak due to graphitic carbon is observed in all XRD patterns, confirming the amorphous nature of the carbon content.

During the carbonization process, the Fe(III) can be partially reduced to Fe(II) by the carbon derived from GCP, which together with the loss of water molecules will lead to formation of empty pores in the crystal structure. As the temperature increases during the carbonization process, the pores generated at lower temperatures start to collapse, leading to the shape

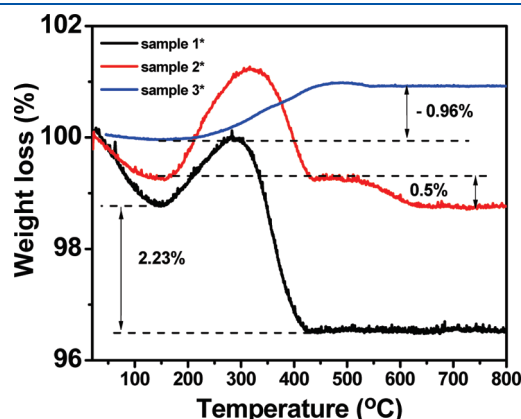


Figure 4. Thermogravimetric analysis (TGA) curves of samples 1*–3*.

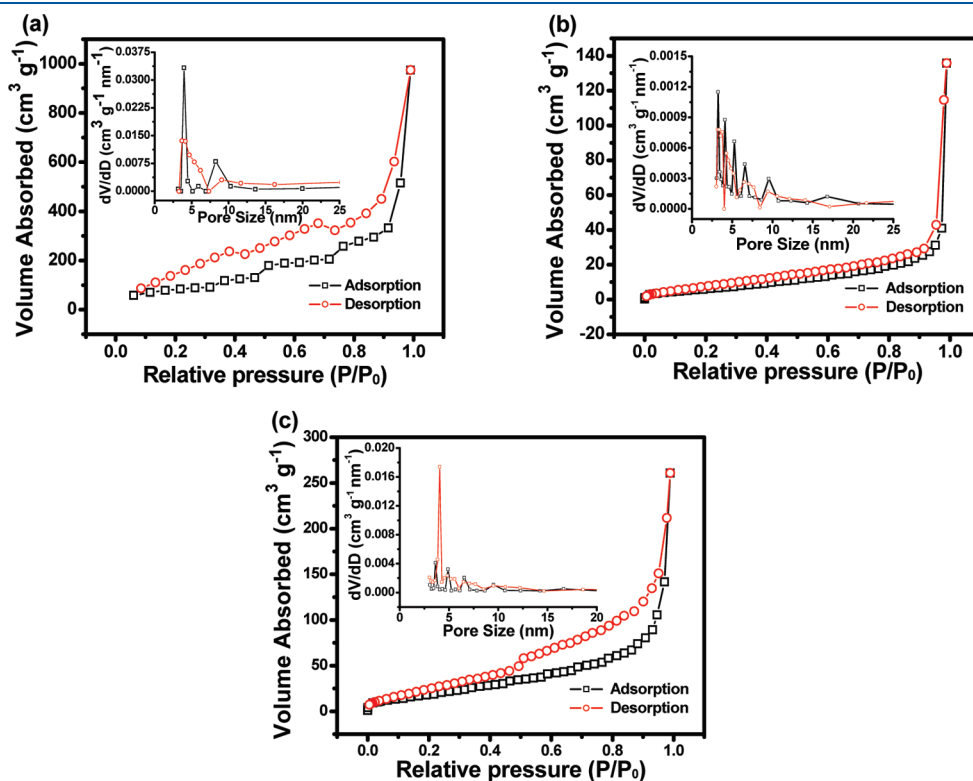


Figure 5. N_2 adsorption–desorption isotherms of samples 1* (a), 2* (b), and 3* (c). The inset in each isotherm is the corresponding pore size distribution.

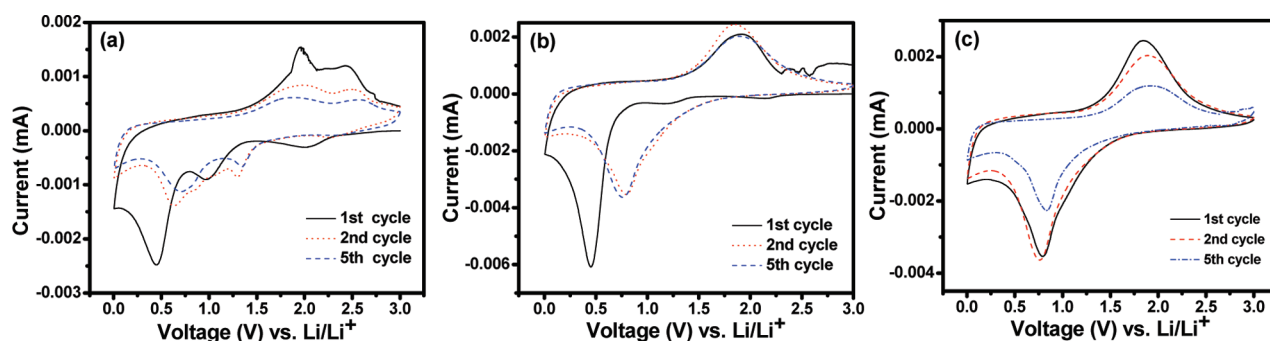


Figure 6. Cyclic voltammograms (CV) of samples 1* (a), 2* (b), and 3* (c) for their first, second, and fifth cycles at a scan rate of 0.5 mV s^{-1} with a voltage window from 3 V to 10 mV.

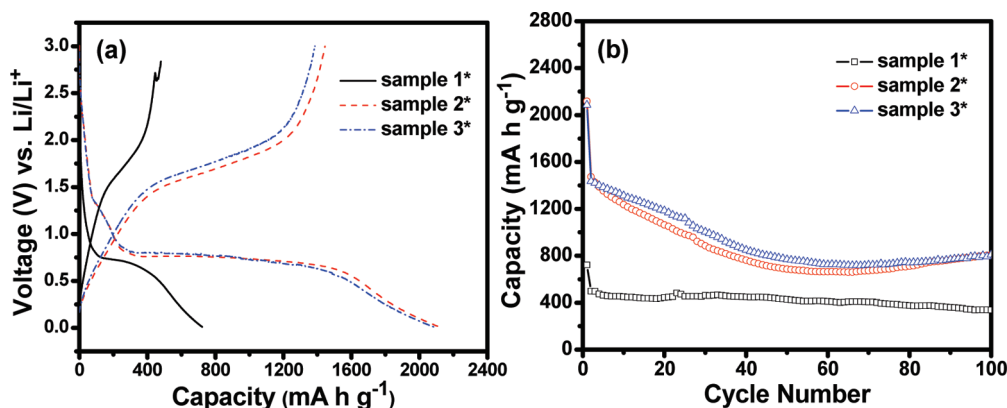


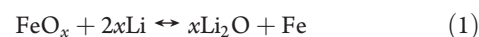
Figure 7. (a) First-cycle charge–discharge voltage profiles for the as-prepared iron oxides. (b) Cyclic performances of samples 1*–3* with the voltage window from 10 mV to 3 V at a current rate of 924 mA g^{-1} .

deformation of the precursor FeOOH nanorods.^{23,24} It is interesting that a distinct carbon nanocoating with a uniform thickness is formed on the formed Fe_3O_4 nanorods after carbonization in samples 2* and 3*. Similar core–shell structures are observed after reduction of SnO_2 –GCP composite nanocolloids.¹⁹ The carbon content in the as-prepared samples is quantitatively determined by thermogravimetric analysis (TGA) (Figure 4). It can be observed that the small weight losses below 150°C are perhaps due to the evaporation of moisture or gaseous contents for all three samples.²⁵ The combustion of carbon begins around 300°C , and the weight changes are nearly completed at about 800°C for all three samples. It should be noted that the Fe_3O_4 can be converted to Fe_2O_3 when heated in air,²⁶ which causes a theoretical weight increase of 3.45% ($1/2 \text{ O}$ is combined for each Fe_3O_4 unit). It can be seen from the curves that the weight increase in samples 1* and 2* completes at around 300°C , while a much higher temperature of nearly 500°C is required for sample 3*. It is speculated that the larger particle size of sample 3* may be responsible for the higher temperature needed to completely convert Fe_3O_4 to Fe_2O_3 . The observed nominal weight losses for samples 1*, 2*, and 3* are 2.23%, 0.5%, and -0.96% , respectively. Hence, on the basis of the above analysis, the weight percentages of carbon content in the as-prepared Fe_3O_4 @C nanocomposites can be easily determined to be about 5.68% for sample 1*, 3.95% for sample 2*, and 2.49% for sample 3*.

Nitrogen adsorption–desorption measurements are carried out at 77 K to study the textural characteristics of the Fe_3O_4 @C samples, as shown in Figure 5, with the insets showing the corresponding Barrett–Joyner–Halenda (BJH) pore size distributions calculated

from both branches of the isotherms. The isotherm profiles of sample 1* and 3* can be categorized as type IV with small hysteresis loops observed at a relative pressure of 0.1–1 for sample 1* and 0.4–1 for sample 3*, while that of sample 2* might be better categorized as type III without a distinct hysteresis loop. The Brunauer–Emmett–Teller (BET) specific surface areas of these three samples are measured to be 296.6, 25.08, and $77.9 \text{ m}^2 \text{ g}^{-1}$ for samples 1*, 2*, and 3*, respectively. The very high surface area of sample 1* may be due to its tiny crystal grains and the highly porous structure that can be observed from the TEM image (see the inset in Figure 3a). It can be observed from the pore size distributions that both samples 2* and 3* have pore sizes in the range of 4–10 nm, while sample 1* has generally smaller pores that are less than 5 nm. The pores generated in all these samples should be attributed to the shrinkage of the GCP layer and recrystallization during the heat treatment.²³

Iron oxides have been widely studied as potential anode materials for lithium ion batteries.^{20,27–29} The electrochemical reaction mechanism of lithium storage in iron oxides can be described as follows:



The formation of Li_2O and Fe is thermodynamically favorable during the discharge process (the forward reaction in eq 1). However, the extraction of Li from Li_2O in the charge process is more difficult, which indicates that a certain extent of irreversibility is inevitable. It was reported that the structure and size of the

iron oxide particles may have crucial effects on the electrochemical performance.^{30,31} Therefore, it is intriguing to investigate the comparative lithium storage properties of the as-prepared three samples with distinct morphologies and sizes.

Here we have investigated the electrochemical properties of samples 1*–3* using two-electrode Swagelok-type cells, where lithium foil serves as both the counter and reference electrodes. Figure 6 shows the cyclic voltammetry (CV) analysis of samples 1*–3* for their first, second, and fifth cycles in the voltage range from 5 mV to 3 V at the same scan rate of 0.5 mV s^{−1}. For sample 1*, two peaks are observed at 0.46 and 1.1 V in the first cathodic polarization process, which could be attributed to the initial lithium insertion into crystal structure and reduction of Fe²⁺/Fe³⁺ to Fe⁰, respectively. An anodic peak is present at 2 V, corresponding to the reversible oxidation of Fe⁰ to Fe³⁺/Fe²⁺. During the subsequent cycles (second and fifth), the peak current decreases significantly in both anodic and cathodic scans, indicating the occurrence of irreversible reactions. Similarly, broad peaks can be clearly found in the cathodic process for sample 2* (0.49 V) and sample 3* (0.76 V). Also, broad peaks centered at about 1.9 V are observed for both samples 2* and 3* during the anodic polarization process, corresponding to the oxidation of Fe⁰ to Fe²⁺/Fe³⁺. In the fifth cycles, both the cathodic and anodic peaks shift to higher potentials, accompanied with decrease of the peak intensity, revealing the certain irreversibility of the redox reactions.

Figure 7a shows the first-cycle charge–discharge voltage profiles of all three samples 1*–3* at a current density of 924 mA g^{−1} (1C). The discharge capacities are observed to be 722, 2117, and 2085 mA h g^{−1} for samples 1*–3*, respectively. From the above TGA analysis, sample 1* contains the highest carbon content. Considering the tiny particle size of sample 1*, it can be deduced that those fine nanoparticles are heavily encapsulated by the amorphous carbon layer. This structural feature might render sample 1* less electroactive. Therefore, its initial capacity is much lower compared to samples 2* and 3*. Subsequently, 488, 1444, and 1385 mA h g^{−1} can be retained in the charge process, indicating irreversible losses of 32%, 31%, and 33% for samples 1*–3*. Figure 7b illustrates the cycling performance of samples 1*–3* with a voltage window from 10 mV to 3 V at a current rate of 1 C. It is obvious from the figure that the capacities increase significantly after 60 cycles for both samples 2* and 3*. We ascribe this phenomenon to a possible activation process. Specifically, after prolonged cycling, the configuration of the Fe₃O₄ electrode might be rearranged, such that the irreversible Li₂O formed during early cycles could be re-exposed and thus participate in the electrochemical reaction. Such a process could even be enhanced by the carbon present in the samples. Thus, this leads to the increase in capacity as the irreversible capacities are partially recovered.^{32,33} For sample 1*, a capacity of 336.8 mA h g^{−1} can be retained after 100 cycles, which indicates a capacity retention of 67.6% (vs the capacity of the second cycle). Very high capacities of 806.6 mA h g^{−1} for sample 2* and 808.2 mA h g^{−1} for sample 3* are obtained after 100 cycles, which suggest their excellent cyclability. Among all the three samples, the stable cycling performance exhibited by sample 1* may be associated with its highest carbon content (recall the TGA results above), which could provide a better cushioning effect that buffers the volume change during the charge–discharge process, leading to improved cyclic capacity retention upon extended cycling.³⁴ On the other hand, with less amount of carbon and better crystallinity, samples 2* and 3* have demonstrated higher reversible capacities than sample 1*.²⁴

Thus, the as-prepared carbon coated magnetite may have potential application in lithium ion batteries.

CONCLUSIONS

In summary, GCP-coated FeOOH nanorods with different aspect ratios and sizes have been successfully synthesized via a facile one-pot hydrothermal method. They can be readily converted into carbon-coated Fe₃O₄ nanorods by heat treatment with little structural alteration. All three Fe₃O₄@C samples are evaluated for their lithium storage properties. A high capacity of over 800 mA h g^{−1} can be retained after 100 cycles. The results show that these carbon-coated magnetite nanocomposites might be used as potential anode materials for high-performance lithium ion batteries.

AUTHOR INFORMATION

Corresponding Author

*E-mail: xwlou@ntu.edu.sg.

ACKNOWLEDGMENT

We are grateful to the Ministry of Education (Singapore) for financial support through the AcRF Tier-1 grant (RG 63/08, MS2120096).

REFERENCES

- (1) Tarascon, J. M.; Armand, M. *Nature* **2001**, *414* (6861), 359–367.
- (2) Whittingham, M. S. *Chem. Rev.* **2004**, *104* (10), 4271–4301.
- (3) Xu, K. *Chem. Rev.* **2004**, *104* (10), 4303–4417.
- (4) Kang, K. S.; Meng, Y. S.; Breger, J.; Grey, C. P.; Ceder, G. *Science* **2006**, *311* (5763), 977–980.
- (5) Armand, M.; Tarascon, J. M. *Nature* **2008**, *451* (7179), 652–657.
- (6) Poizot, P.; Laruelle, S.; Grugeon, S.; Dupont, L.; Tarascon, J. M. *Nature* **2000**, *407* (6803), 496–499.
- (7) Arico, A. S.; Bruce, P.; Scrosati, B.; Tarascon, J. M.; Van Schalkwijk, W. *Nat. Mater.* **2005**, *4* (5), 366–377.
- (8) Han, S. J.; Jang, B. C.; Kim, T.; Oh, S. M.; Hyeon, T. *Adv. Funct. Mater.* **2005**, *15* (11), 1845–1850.
- (9) Lou, X. W.; Yuan, C.; Zhang, Q.; Archer, L. A. *Angew. Chem., Int. Ed.* **2006**, *45* (23), 3825–3829.
- (10) Na, H. B.; Song, I. C.; Hyeon, T. *Adv. Mater.* **2009**, *21* (21), 2133–2148.
- (11) Huo, L. H.; Li, W.; Lu, L. H.; Cui, H. N.; Xi, S. Q.; Wang, J.; Zhao, B.; Shen, Y. C.; Lu, Z. H. *Chem. Mater.* **2000**, *12* (3), 790–794.
- (12) Gondal, M. A.; Hameed, A.; Yamani, Z. H.; Suwaiyan, A. *Chem. Phys. Lett.* **2004**, *385* (1–2), 111–115.
- (13) Noh, M.; Kwon, Y.; Lee, H.; Cho, J.; Kim, Y.; Kim, M. G. *Chem. Mater.* **2005**, *17* (8), 1926–1929.
- (14) Wang, Y.; Zeng, H. C.; Lee, J. Y. *Adv. Mater.* **2006**, *18* (5), 645.
- (15) Cao, Q.; Zhang, H. P.; Wang, G. J.; Xia, Q.; Wu, Y. P.; Wu, H. Q. *Electrochem. Commun.* **2007**, *9* (5), 1228–1232.
- (16) Hu, Y. S.; Guo, Y. G.; Dominko, R.; Gaberscek, M.; Jamnik, J.; Maier, J. *Adv. Mater.* **2007**, *19* (15), 1963.
- (17) Zhang, W. M.; Wu, X. L.; Hu, J. S.; Guo, Y. G.; Wan, L. J. *Adv. Funct. Mater.* **2008**, *18* (24), 3941–3946.
- (18) Cui, Z. M.; Hang, L. Y.; Song, W. G.; Guo, Y. G. *Chem. Mater.* **2009**, *21* (6), 1162–1166.
- (19) Lou, X. W.; Chen, J. S.; Chen, P.; Archer, L. A. *Chem. Mater.* **2009**, *21* (13), 2868–2874.
- (20) Nuli, Y. N.; Zhang, P.; Guo, Z. P.; Liu, H. K. *J. Electrochem. Soc.* **2008**, *155* (3), A196–A200.
- (21) Zeng, S. Y.; Tang, K. B.; Li, T. W.; Liang, Z. H.; Wang, D.; Wang, Y. K.; Qi, Y. X.; Zhou, W. W. *J. Phys. Chem. C* **2008**, *112* (13), 4836–4843.

- (22) Lou, X. W.; Li, C. M.; Archer, L. A. *Adv. Mater.* **2009**, *21* (24), 2536.
- (23) Piao, Y.; Kim, J.; Bin Na, H.; Kim, D.; Baek, J. S.; Ko, M. K.; Lee, J. H.; Shokouhimehr, M.; Hyeon, T. *Nat. Mater.* **2008**, *7* (3), 242–247.
- (24) Piao, Y. Z.; Kim, H. S.; Sung, Y. E.; Hyeon, T. *Chem. Commun.* **2010**, 46 (1), 118–120.
- (25) Chen, J. S.; Tan, Y. L.; Li, C. M.; Cheah, Y. L.; Luan, D.; Madhavi, S.; Boey, F. Y. C.; Archer, L. A.; Lou, X. W. *J. Am. Chem. Soc.* **2010**, *132* (17), 6124–6130.
- (26) Deng, H.; Li, X. L.; Peng, Q.; Wang, X.; Chen, J. P.; Li, Y. D. *Angew. Chem.-Int. Ed.* **2005**, *44* (18), 2782–2785.
- (27) Wang, S. Q.; Zhang, J. Y.; Chen, C. H. *J. Power Sources* **2010**, *195* (16), 5379–5381.
- (28) Kim, H. S.; Piao, Y.; Kang, S. H.; Hyeon, T.; Sung, Y. E. *Electrochem. Commun.* **2010**, *12* (3), 382–385.
- (29) Chen, J. S.; Zhu, T.; Yang, X. H.; Yang, H. G.; Lou, X. W. *J. Am. Chem. Soc.* **2010**, *132*, 13162–13164.
- (30) Grugeon, S.; Laruelle, S.; Herrera-Urbina, R.; Dupont, L.; Poizot, P.; Tarascon, J. M. *J. Electrochem. Soc.* **2001**, *148* (4), A285–A292.
- (31) Larcher, D.; Masquelier, C.; Bonnin, D.; Chabre, Y.; Masson, V.; Leriche, J. B.; Tarascon, J. M. *J. Electrochem. Soc.* **2003**, *150* (1), A133–A139.
- (32) Do, J.-S.; Weng, C.-H. *J. Power Sources* **2005**, *146* (1–2), 482–486.
- (33) Wu, P.; Du, N.; Zhang, H.; Yu, J.; Yang, D. *J. Phys. Chem. C* **2011**, *115* (9), 3612–3620.
- (34) Liu, H.; Wang, G. X.; Wang, J. Z.; Wexler, D. *Electrochem. Commun.* **2008**, *10* (12), 1879–1882.